Remote Sensing of Environment 158 (2015) 1–14

Contents lists available at ScienceDirect

Remote Sensing of Environment

journal homepage: www.elsevier.com/locate/rse

Estimating advective near-surface currents from ocean color satellite images

Haoping Yang [a,*], Robert Arnone [a], Jason Jolliff [b]

[a] University of Southern Mississippi, Stennis Space Center, MS 39529, USA
[b] Naval Research Laboratory, Stennis Space Center, MS 39529, USA

ARTICLE INFO

Article history:
Received 29 July 2014
Received in revised form 22 October 2014
Accepted 11 November 2014
Available online 1 December 2014

Keywords:
MCC
Ocean color
Surface advection
HFRadar currents
BioCast experiment
Bio-optical
VIIRS
Overlap of swath
Image-derived currents
Synthetic velocity

ABSTRACT

Improved maximum cross correlation (MCC) techniques are used to retrieve ocean surface currents from the sequential ocean color imagery provided by multiple newer generations of satellite sensors on hourly scales in the Yellow Sea and the U.S. East and Gulf coasts. The MCC calculation is validated in a series of Bio-Optical Forecasting (BioCast) experiments with predetermined synthetic velocities, and its products are evaluated by examining the errors and biases with respect to the High Frequency Radar (HFRadar) measurements. The root-mean-square (RMS) errors in our best current products derived from the overlap of satellite sensor swath between the VIIRS sequential orbits are less than 0.17 m s^{-1} in the evaluation area outside of the Chesapeake Bay. The most accurate current products are those derived from the imagery data of $R_{rs}(551)$, $B_b(551)$ and $C(551)$, while the image sequences of $B_b(551)$ and Z_{eu}_lee are identified as the most suited products for the retrieval of currents because of their best production capacities of valid velocity vectors. Mechanisms between the advective processes and the dynamic changes of bio-optical properties are discussed regarding the performances of various color products on the retrieval of currents. Similarities of velocity distribution in the retrieved vector arrays are collected across different MCC products derived from ocean color datasets that are of different types and derived from different spectral channels of satellite overpasses. The inter-product similarities themselves can be used to characterize the near-surface advection as well and usually have smaller errors than each of the individual MCC currents. Moreover, efforts are also under way to improve the ocean color derived currents by merging several of the MCC products with similarities to increase the total spatial coverage. This study not only seeks the image-derived products best representing the sea surface current structures in coastal areas, but also exploits how these currents can be improved or optimized to support the ocean forecasts.

1. Introduction

The retrieval of surface currents from time sequential satellite imagery has been demonstrated using the maximum cross correlation (hereafter MCC) method by many researches (Emery, Fowler, & Clayson, 1992; Emery, Thomas, Collins, Crawford, & Mackas, 1986; Matthews & Emery, 2009; Wahl & Simpson, 1989, 1990, 1991; Wu, Pairman, McNeill, & Barnes, 1992; Zavialov, Grigorieva, MoLler, Kostianoy, & Gregoire, 2002, etc.). Most of these studies were focused on estimating currents from thermal imagery by the implementation of MCC method and its variants. Although the basic rules are similar, the detailed implementation of this method varied from case to case in the documented studies. For example, Emery et al. (1992) applied statistical significance and next-neighbor filter techniques to remove fictitious current vectors due to the presence of residual clouds; Wahl and Simpson (1991) indirectly estimated the tangential component of the total flow based on vector subtracting of the total flow and the normal component of flow; Zavialov et al. (2002) developed a modified version of the MCC method by allowing small displacements along isolines to be detected between the paired images.

Besides the cross-correlation based methods, several other approaches have been proposed in the literature for extracting the near-surface currents as well. The optical flow algorithm (Horn & Schunck, 1981) is a variational approach with a framework where the optical flow is computed as the solution of a minimization problem. Cote and Tatnall (1994) proposed a different pattern matching method named as Hopfield neutral network to estimate feature movement, which allows the deformation of pattern title and is faster than the conventional cross-correlation based methods. To overcome some weaknesses of the MCC method (e.g. Kamachi, 1989 pointed out the deficiency of not reconstructing rotational and deformational motion patterns), Bannehr, Rohn, and Warnecke (1996) presented a non-statistical functional analytic method to derive displacement vector field under the consideration of neighborhood information.

* Corresponding author at: Department of Marine Sciences, University of Southern Mississippi, Stennis Space Center, MS 39529, USA. Tel.: +1 786 376 6450.
E-mail address: Haoping.Yang@gmail.com (H. Yang).

http://dx.doi.org/10.1016/j.rse.2014.11.010
0034-4257/

In some previous studies (e.g. Chen, Mied, & Shen, 2008; Emery et al., 1992; Vigan, Provost, Bleck, & Courtier, 2000a, 2000b), the derived currents were compared to the ocean model velocity field to examine errors and uncertainties. However, it must be noted that in many situations the velocity outputs from ocean circulation models can be misrepresented because most of the present-day operational ocean models do not assimilate velocity observation and there are often large inter-model differences in the velocity products of different ocean models. Although the large regional scale ocean current observations are a limitation for validation of models especially in remote regions, the development of the HFRadar network as a part of the U.S. coastal observing system has somehow improved this situation. The HFRadar measurement of sea surface currents is being used increasingly in the U.S. coastal waters and regularly provides hourly velocity observation in several spatial resolutions. In the study of the U.S. coastal waters, we no longer evaluate the derived currents with respect to the ocean model currents but instead compare them to the velocities derived by the HFRadar network. In our BioCast experiment, the image-derived currents are directly compared to the pre-established synthetic velocities to validate the retrieval procedure.

The time span between the sequential satellite images should impact the frontal movements associated with ocean processes such as tides, winds and eddies. In coastal areas, river plume fronts are rapidly changing movements and require approximately ~1 hour separation between images. Comparatively, gulf stream and large eddies can have longer time periods, such as days, to response the surface currents.

Sea surface temperature (SST) is a physical parameter that has a direct link to the advection processes and frontal movements and has long been used to track and estimate the surface currents. However, there are issues such as the diurnal heating of surface water, that have influence on the location of frontal movement and thereby the ability to derive currents. The SST products are also limited to time of the year when there are significant gradients for frontal detection. In summer months, not only are there large temperature variations during a full heating and cooling cycle, but also the strong radiance could significantly change the stratification near the sea surface and smooth out many small-scale information which are essentially preferred in executing a typical MCC calculation. In the Gulf of Mexico during the summer months, for example, the SST is sometimes isothermal and can neither resolve frontal location nor be used for defining the surface currents.

The tracking of ocean color fronts such as the chlorophyll fronts from sequential satellite images can also be used to track water mass advection (Crocker, Matthews, Emery, & Baldwin, 2007; Garcia & Robinson, 1989; Svejkovsky, 1988). However, bio-optical products are also influenced by non-advective processes such as growth and decay of phytoplankton blooms which can impact the gradients and frontal locations and thereby the ability to estimate surface movements. These bio-optical processes are dependent on the timing between the sequential images and are assumed to be negligible with the hours (Dickey et al., 1991), therefore the velocity products retrieved from hourly sequential images can be used to represent the advective processes. Besides chlorophyll, there are many ocean color products available which respond to different bio-optical and advective processes, some of which may be more optimally suited for retrieving currents. An inter-product comparison can help identify both the similarities and differences of velocity distribution among various ocean color derived velocity products. On the grounds that these separately derived MCC products are used to represent the same surface advection, it is the inter-product similarities, instead of the differences, that are more likely to link with the surface flow. Because of this, we may not only use the similarities themselves to estimate advective processes besides the individual MCC products, but also merge the multiple MCC products by keeping both their similarities and differences to increase the total spatial coverage of velocity field. One primary reason for carrying out this study is that we can take advantage of the abundance of available ocean color satellite products to support the timely forecasts and the coastal operations in need of surface current information.

The present study uses the sequential ocean color products provided by the Geostationary Ocean Color Imager (GOCI) and Visible Infrared Imaging Radiometer (VIIRS). The visible and infrared spectra measured from these satellite instruments can provide information about dissolved and suspended constituents in water that have optical properties. Many of their remotely sensed products can help define the surface circulation features and one effective way is to use these products to retrieve the advective currents by image processing algorithms such as the MCC method. The objectives of this paper include the following: 1) applying MCC to various ocean color products and evaluating the derived currents to define the optimum products which are best related to surface advection; 2) testing the MCC algorithms for ocean color products using synthetic datasets that are initialized with chlorophyll data and based on a forecast circulation model; 3) demonstrating the retrieval of currents from the VIIRS overlaps; 4) determining the uncertainty and RMS error of the derived currents by comparing with the observed currents from HFRadar network; 5) illustrating that similarities of velocity distribution can be collected through different MCC currents derived from different ocean color products and how these MCC currents with similarities may be merged to increase the total spatial coverage.

In Section 2, the satellite imagery data and the velocity estimating methods are briefly introduced. Case studies of the BioCast experiment follow in Section 3 to validate the MCC retrieval procedure. Section 4 gives an example to illustrate that the high similarities of velocity distribution can be collected between the currents derived from different ocean color products. The evaluation of MCC products in the U.S. East and Gulf coasts with respect to the HFRadar measurements is presented in Section 5. Section 6 describes some techniques of merging multiple derived currents to improve the vector coverage of flow field. The concluding remarks are given in Section 7.

2. Data and approaches

2.1. GOCI and VIIRS satellite imagery

The ocean color imagery used in this study is obtained from the remotely sensed data of the GOCI and VIIRS, which are capable of providing multiple looks per day for each of a number of different types of bio-optical properties. GOCI is a sensor on a Korean telecommunications satellite (i.e. the Communication, Ocean and Meteorological Satellite-1, COMS-1); VIIRS is a sensor on the Suomi National Polar-Orbiting Partnership (S-NPP) satellite. The GOCI is the world's first geostationary orbit satellite sensor over the Yellow Sea for detecting, monitoring and predicting short-term biophysical phenomena. The target area is 2500 km × 2500 km and centered at 130°E, 36°N; a map of its coverage can be found at http://kosc.kordi.re.kr/oceansatellite/coms-goci/specification.kosc. Hourly data for 9 am–3 pm daily are acquired in multispectral bands from 412 to 865 nm and with a spatial resolution of about 500 m. The GOCI can capture the hourly images eight times per day, which is very useful to learning the evolution of the dynamic changes in water masses and bio-optical properties, particularly in coastal waters where the river discharge, tides, winds, and the shape of land and seafloor all play a role in shaping the surface flow.

The VIIRS is a polar orbiting satellite sensor with a 22-band radiometer for collecting imagery and radiometric measurements of the ocean in the visible and infrared bands of electromagnetic spectrum. The VIIRS orbit provides an overlap of the sensor swath so that multiple looks per day and bio-optical products can be collected over the same ocean (Arnone et al., 2013). The overlap between VIIRS sequential orbits is about 100 min and based on the orbital progression. The overlap of VIIRS at the U.S. East coasts does not occur every day. There is enough overlap in this area approximately every 2 days. In Northern hemisphere the spatial resolution increases with latitude and is approximately 750 m at nadir in the U.S. East and Gulf coasts but 1.6 km at

the edge of the swath. The VIIRS has a 3040 km swath and the orbital overlap is determined by the edge of swath. The VIIRS sensor has the uniquely increased ability to retain spatial resolution of 750 m at NIDAR to small spatial increase at higher swath angles (Baker, 2011). An example of VIIRS overlap is shown in Fig. 1.

The GOCI and VIIRS produce images from their data which are then converted into geophysical data products. The satellite data was processed using the NASA based software called nL2gen (Werdell et al., 2013) to remove the atmosphere contamination, surface glints, etc. The nL2gen uses multiple channels. The derived ocean color products include the normalized water leaving radiance L_{wn} at several wavelengths. These spectral L_{wn} channels are used to derive several in-water bio-optical properties (Lee, Carder, & Arnone, 2002). The sensed data of the GOCI and VIIRS provide a series of ocean color products that are of different types and derived from multiple spectral channels. These products are presented in Table 1, in which the special attention is given to the 551 nm products. The VIIRS channel M4 is centered at visible 551 nm; the GOCI band 4 is also centered at 551 nm. After the atmospheric correction and ocean color processing produces, the $L_{wn}(551)$ would be seen directly from overhead and not for an off angle. The L_{wn} at the different channels provide a spatially normalized product which is used for quantitative comparison across the scene. In coastal areas where there are large concentrations of inorganic particles (suspended sediment), there is increased scattering which is detected in the $L_{wn}(551)$ and the backscattering products. A hypothesis is that some of these products are better indications of the water mass advection than the others. For example, the blue channels were selected to define the bio-optical response of chlorophyll absorption whereas the longer green and red channels characterize the particle scattering properties. We expect that the green 551 channel has a signature to better characterize and identify water masses using the particles scattering compared to the red channels and is better to define advection than other bio-optical properties used in ocean color.

For both GOCI and VIIRS, the ocean color products were remapped to a specific projection (level 3) with equal grid spacing. This was performed to provide spatially consistent grids across the swath of the satellite. The MCC analysis is carried out on remapped images.

2.2. MCC approach

The MCC method for determining surface currents from time sequence images is based on statistically characterizing the spatial gradients between images. It calculates the displacement of small regions of patterns from one image to another to find the movement of surface features by locating the correlation peaks in windowed portions of the source images. By statistically characterizing the spatial gradient of one image and locating the position of the similar statistics in the second image we can track the location of a water mass from one time to the next. The displacement during the time interval provides both the magnitude and direction of the surface current. The method requires identifying the correct spatial (pattern box size) variability and the pattern difference requires variance to accurately locate the movements. These statistics also provide methods to track the level of uncertainty of the derived current. The schematics of the MCC method are illustrated in Fig. 2. More details of this method can be found in Emery et al. (1986), Garcia and Robinson (1989), Wahl and Simpson (1990), and Wu et al. (1992).

Assuming that there is a pattern movement of m pixels in x-direction and n pixels in y-direction from the first image to the second, the cross-correlation coefficient between the two pattern tiles is determined by

$$k = \frac{\sum_i \sum_j [\varphi_2(i+m, j+n) - \overline{\varphi}_2(i+m, j+n)]\,[\varphi_1(i,j) - \overline{\varphi}_1(i,j)]}{\sqrt{\sum_i \sum_j [\varphi_2(i+m, j+n) - \overline{\varphi}_2(i+m, j+n)]^2 \sum_i \sum_j [\varphi_1(i,j) - \overline{\varphi}_1(i,j)]^2}}, \quad (1)$$

where φ_1 (φ_2) is the value of the target variable on the first (second) image; i and j the indices of the pattern tile on the first image; $i + m$ and $j + n$ the indices of the corresponding pattern on the second image; and $\overline{\varphi}_1$ ($\overline{\varphi}_2$) the tile-wide mean on the first (second) image.

The results of the MCC algorithm provide several outputs, which include the direction and magnitude of the surface current. In addition to the pattern similarity in the matchup statistics between the two images, the level of cross-correlation represents a degree of confidence in the retrieved currents. If the statistics fall below a certain threshold then a surface current is not determined. This provides a method to qualify the current product.

To best estimate the near-surface currents, the ocean color imagery data should be ideally free of clouds and other contamination, but it is not usually possible. The scenes were processed using standard (Gordon & Wang, 1994) atmospheric correction; standard flags were used to mask interference from land, clouds, sun glint, and other potential disturbances to the radiance signal. These are based on thresholds in the 865 nm channel and are standard processing methods used in NASA processing (Werdell et al., 2013). Technically, the MCC approach cannot get any valid velocities if the area is covered by heavy clouds. However, for some sparsely distributed cloudy pixels, we may apply low pass filter

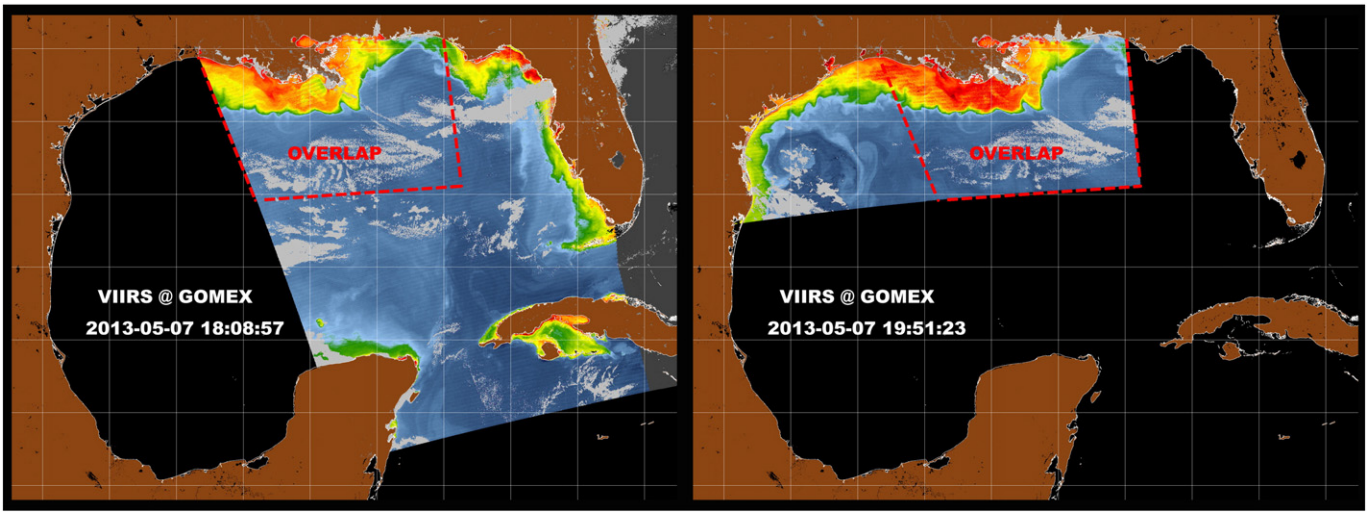

Fig. 1. An example of the VIIRS overlap illustrating that sequential imagery data with ~100 min separation may be available in the overlapped region of the polar orbiting SNPP-VIIRS sensor swath. The boundary of the overlapped area is indicated by the dashed lines, which are the same on both images.

Table 1
Selected ocean color products of the GOCI and VIIRS in the present study.

Satellite sensor	GOCI	VIIRS
Spatial resolution (m)	500	750
Temporal resolution (min)	60	100
Ocean color products	Chl, $L_{wn}(551)$	$R_{rs}(410)$, $R_{rs}(443)$, $R_{rs}(486)$, $R_{rs}(551)$, $R_{rs}(671)$, $A_t(551)$, $B_b(551)$, C(551), Chl, $K_d(490)$, salinity, Z_{eu}_lee

Abbreviation and description of the above-presented ocean color parameters:
$A_t(551)$: total absorption at 551 nm, QAA algorithm; $B_b(551)$: total backscatter at 551 nm, QAA algorithm; C(551): beam attenuation at 551 nm, QAA algorithm; Chl: chlorophyll *a* concentration; $K_d(490)$: diffuse attenuation coefficient at 490 nm, KD2 algorithm; $L_{wn}(551)$: normalized water-leaving radiance at 551 nm; $R_{rs}(\lambda)$ (λ = 410, 443, 486, 551, 671): remote sensing reflectance at 410, 443, 486, 551, and 671 nm; Salinity: salinity — based on colored dissolved organic matter, Ladner algorithm; Z_{eu}_lee: euphotic zone depth, Lee algorithm (Lee et al., 2007).

to smooth out the bad values before the MCC calculation is conducted. The smoothing of source images can generally increase the production of valid vectors and is routinely used in our studies. Another pre-processing technique that we used is the mesh refinement with interpolation techniques such as the bi-linear interpolation that will be discussed later in the section of BioCast experiment.

An unfiltered current product retrieved by MCC algorithm may contain plenty of unrealistic vectors. Diagnostic analysis suggests that these vectors are possibly caused by several factors including the following: 1) the bad pixels existing in satellite source imagery, 2) the misrepresentation of some movement of pattern features particularly in the case that there are large angular displacements due to the rotational motions of layered fluids, and 3) the fact that the real sea surface currents themselves have plenty of turbulent features. To weaken the negative aspects in the derived currents, we have essentially enabled several types of filters: the land mask filter screens out the vectors on land areas; the neighborhood filter double checks whether a vector is physically compatible with the other vectors calculated on the adjacent pixels; the gradient filter rejects the vectors retrieved from pattern pairs that do not have sufficient spatial and temporal variability; the MCC threshold filter discards some of the results retrieved from weakly correlated local patterns by excluding the vectors with peak correlation values k_{max} smaller than the cutoff threshold k_σ.

2.3. Metrics for quantifying the skills of the derived current

The evaluation of the derived currents for different MCC criteria and ocean color sequences was based on:

- Number of current vectors retrieved that satisfy the criteria $k_{max} \geq k_\sigma$: The more vectors retrieved the better the current product is. The ocean color images with the capacity of producing larger quantity of valid vectors are more suited for the retrieval of currents.
- Variance of velocity difference var($\mathbf{U}_1 - \mathbf{U}_2$): This parameter measures the similarity level of velocity distribution between two currents $\mathbf{U}_1$ and $\mathbf{U}_2$, which are derived from two different color products such as Chl and $L_{wn}(551)$.
- RMS error: This parameter is a measure of accuracy and represents the sample standard deviation of the differences between MCC derived currents and those observed by HFRadar.
- Bias: A statistic measure of how the derived currents are systematically different from the observed currents. A small bias can guarantee

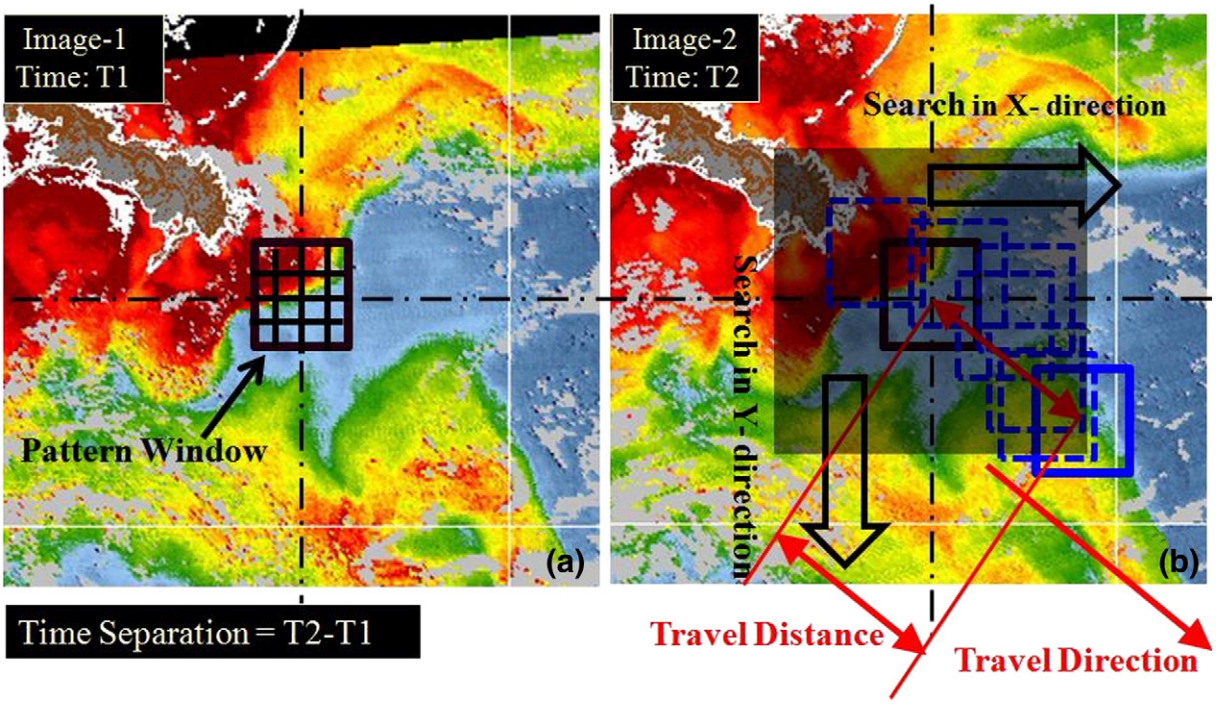

Fig. 2. Schematics of the MCC algorithm. Two sequential ocean color images are used to estimate surface currents by the MCC method. The gridded box on image-1 is the original pattern tile at T_1. On image-2, the pattern tile is allowed to move away from the target pixel in both *x*- and *y*-directions. The dashed line boxes in blue are the possible new states of the original pattern at T_2. *Assuming* that the bold solid box in blue has the largest cross-correlation with respect to the original pattern, the advective velocity is then determined by the time separation $T_2 - T_1$, the travel distance and the travel direction. The shadow area in Fig. 2b is the search window.

that the derived currents are not unrealistically overestimated or underestimated.

Particularly, the RMS error and bias are calculated as,

$$\varphi_{\mathrm{RMS}} = \sqrt{\frac{1}{N}\sum_{i=1}^{N}(\hat{\varphi}_i - \varphi_i)^2} \text{ and } \varphi_{\mathrm{bias}} = \frac{1}{N}\sum_{i=1}^{N}(\hat{\varphi}_i - \varphi_i), \quad (2)$$

where N is the number of pixels loaded with both the observed vectors and the vectors retrieved from MCC; i the index of pixel; $\hat{\varphi}$ the scalar value extracted from the MCC current product (specifically, $\hat{\varphi}$ may be the magnitude, direction, u-component or v-component of the surface current); and φ the observed value of $\hat{\varphi}$.

3. BioCast experiment

The BioCast system has been used to forecasting the ocean's optical environment (Jolliff et al., 2014) and the nowcast–forecast studies of ocean color data streams in physical circulation models (Jolliff, Smith, Ladner, & Arnone, 2014). We apply the BioCasting technique to a validation study in which a synthetic dataset was established to test the MCC algorithm on ocean color products. A surface circulation model with a specific constant current vector was used to advect a selected satellite product (such as Chl) to obtain a sequence of synthetic forecast states with 100 min separation. By using these states as an artificial image sequence, the MCC was applied to determine if it could retrieve the constant vector field. The synthetic velocities are functionally the pre-established observation, and we can thus use them to quantify the accuracy of the velocities derived from the artificial image sequence as well as to validate the calculation.

3.1. Case studies

We present five test cases built from the BioCast software, in each case the Chl field moves with a constant synthetic velocity so the continuity is automatically satisfied in water masses. Specifically, multiple constant velocities are separately loaded to a given initial field of Chl to yield several different artificial image sequences. The synthetic velocities in our BioCast experiment are listed in Table 2. The same initial field, which is a real Chl image captured from the VIIRS, is used here to obtain all the five artificial sequences. The spatial and temporal resolutions are 1000 m and 100 min, respectively. An artificial image sequence in the Northern Gulf of Mexico is shown in Fig. 3 for $u = 0.5$ and $v = -0.5$ m s^{-1} (i.e., case 3 in Table 2) as an example. The image sequence may also be recognized as a consequence of fixed lands superimposing with an ocean color map that moves at a constant velocity. The image-derived currents by MCC are presented in Fig. 4, in which the retrieved vectors are visually realistic with respect to the corresponding predetermined velocities.

3.2. RMS error and bias

We examine the RMS errors and biases of the image-derived velocity products that are described in Table 2. The results are presented in Table 3 for the u- and v-components, in which the RMS errors are less than 0.1 m s^{-1} in all the studied cases and the biases are within ± 0.03 m s^{-1}. The results of the magnitude and direction are given in Table 4.

Table 2
Predetermined velocities in the five case studies of the BioCast experiment. The direction angle θ is measured from the positive x-axis in the counterclockwise direction.

BioCast test	1	2	3	4	5
Zonal velocity u (m s^{-1})	−0.2	0.2	0.5	−0.5	0.5
Meridional velocity v (m s^{-1})	−0.2	0.2	−0.5	0.5	0.001
Direction of velocity vector θ (°)	225	45	315	135	0.1

In a MCC retrieval procedure, both the magnitude and direction are restricted by the spatial resolution of the source images. The displacement of pattern center must have its initial position at one pixel grid on the first image and the final position at another pixel grid on the next image. Due to the fact that the pixel grids are discrete in space, this intrinsic constraint could somehow lead to systematic errors due to the limited pixel resolution. To weaken this limitation, we tentatively refine the source images by reducing the pixel size to half of the original and then redo the MCC calculation. Subsequently, the errors in the MCC currents derived from both the refined and non-refined images are presented in Fig. 5 to show the impact of mesh refinement. The curves in Fig. 5b exhibit quantitatively similar behaviors as in Fig. 5a calculated on the original meshes. For the velocities u and v, it is clear that the bi-linear interpolation based mesh refinement does not reduce the RMS errors on almost all the cases, but the overall biases are weakened from [−0.032, +0.030] to [−0.015, +0.015] m s^{-1} as shown in Fig. 5c and d. The largest bias correction occurs in test 1 when $u = -0.2$ and $v = -0.2$ m s^{-1}. In this case, the refinement of source imagery reduces the bias from +0.029 m s^{-1} to +0.009 m s^{-1} with a correction of ~69%. Moreover, the RMS errors and biases of the velocity magnitude and direction are presented in Fig. 5e through h, which again shows that the bi-linear interpolation corrects the biases but not the RMS errors. This is probably because the Chl values on the "new pixels" resulting from interpolation might not be able to accurately represent the pattern features statistically matched up with the remotely sensed values on the original pixels. The bi-linear interpolation, which is one of the basic resampling techniques, does not reduce the error here in the MCC derived currents, but by no means that other non-linear interpolation algorithms cannot yield an error reduction. In a companion study, for example, we have been attempting to calculate the surface currents from the refined images produced by band-sharpening techniques and the results will be reported separately when completed. As a generalization, Fig. 5 indicates that the MCC algorithm yields the RMS errors of less than 0.11 m s^{-1} in velocity components and less than 12° in velocity direction for sequential images with 100 min separation when the template size and axial searching distance are set to 6 × 6 pixel and 12 pixel, respectively.

4. Similarity in the MCC currents derived from different ocean color products

Satellite remote sensing can provide many ocean color products that are of different types and derived from different spectral channels. The imagery of each of the many products may be separately used to retrieve the surface currents. Due to the fact that every individual color product may theoretically obtain a deterministic derived velocity product for its own, there is the question of which derived product should be chosen to represent the surface flow out of the many velocity products that are usually sort of different from each other. To reduce the overall risk of making a particularly poor selection, we need to investigate the similarities and differences of velocity distribution between the multiple derived currents, which is particularly necessary if there are no observed currents available. As mentioned in the Introduction section, because the different MCC products are intentionally obtained to represent the same surface flow, it is the inter-product similarities, instead of the differences, that are more likely to stand for the surface advection. If high similarities can be identified between the different current products, then these similarities should be able to characterize the surface flow, and the individual products with similarities are potentially good candidates as well for representing the surface flow. Assuming that there are two currents derived from two different ocean color products; if the two derived currents are completely different, then at least one of the two ocean color products is not suited for the retrieval of currents because the two derived currents are tentatively representing the same thing. Below we take two MCC products retrieved

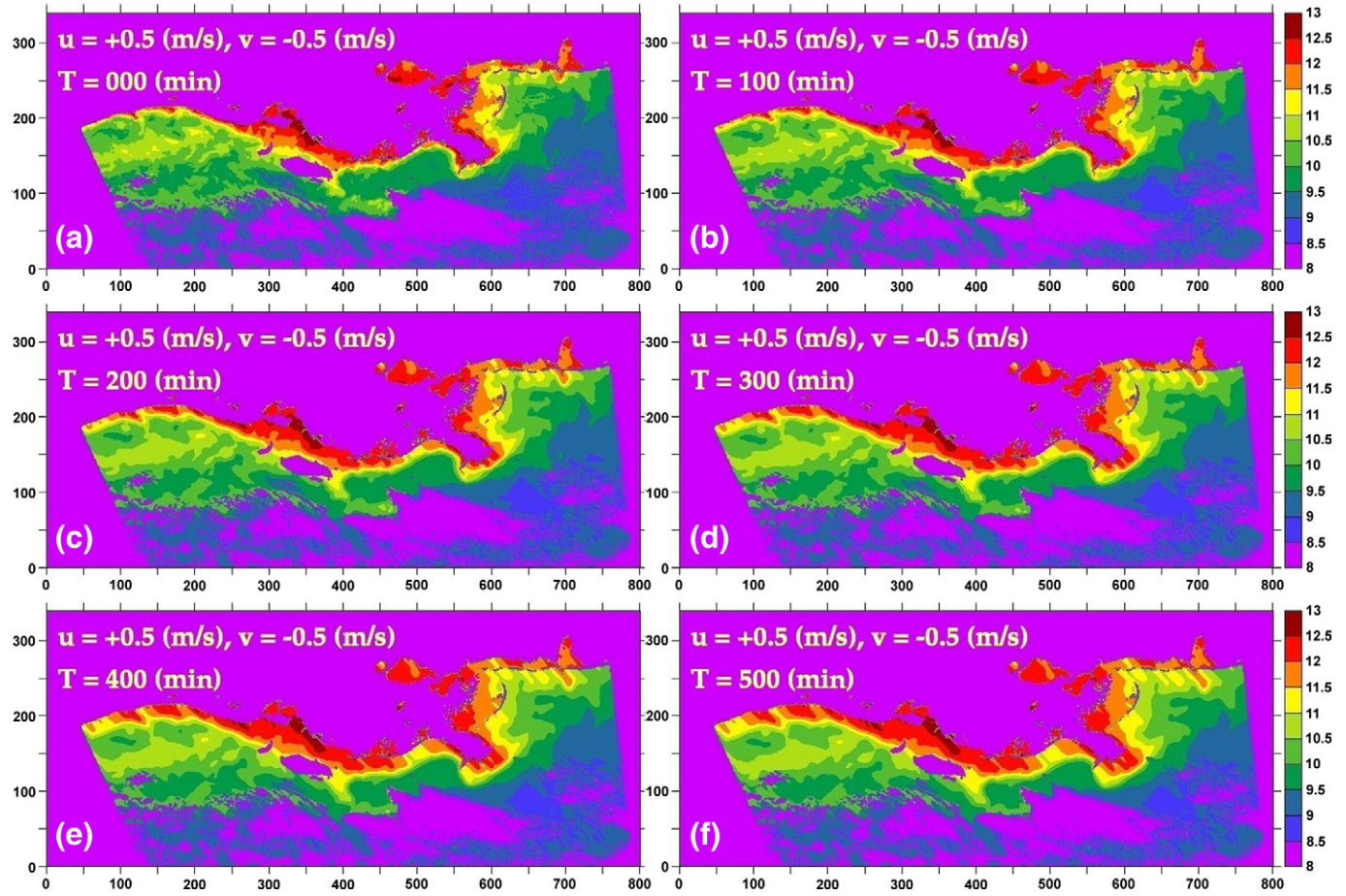

Fig. 3. Artificial image sequence constructed in the BioCast experiment for $u = +0.5$ and $v = -0.5$ m s^{-1} at the time of $T =$ (a) 0, (b) 100, (c) 200, (d) 300, (e) 400 and (f) 500 min. The spatial resolution of the images is 1000 m.

from the GOCI's Chl and $L_{wn}(551)$ imagery as an example to show the similarity existing between the MCC currents resulting from different ocean color products.

The Chl fields In Fig. 6a and c are presented for 02:16 UTC and 03:16 UTC on September 6th, 2011. Heavy clouds are observed in the west coast particularly in the near-shore regions of Bo Hai Bay and south of 35.5°N. The relatively larger spatial gradients are distributed in the east coasts in comparison to the open ocean. The currents estimated by MCC algorithm are shown in Fig. 6e, in which plenty of the MCC current vectors are northwards in the north of the Yellow Sea and along the east coast, while those in the areas near the southern corner of the Korean Peninsula are southeastwards. These are in visual agreement with the movement of pattern features between the two Chl images.

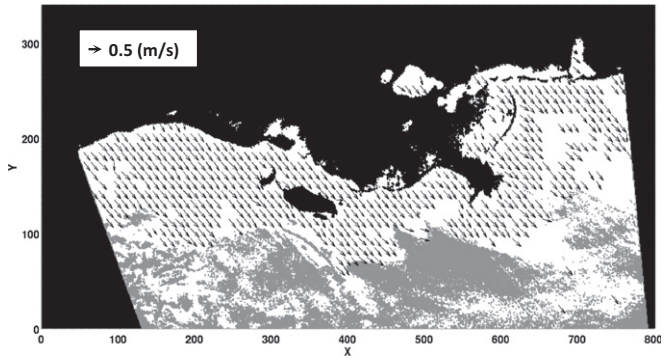

Fig. 4. Image-derived currents by the MCC algorithm from the artificial image sequence corresponding to $u = 0.5$ m s^{-1} and $v = -0.5$ m s^{-1}. The vector field is bin-averaged from a total of 114,907 valid vectors. The threshold $k_\sigma = 0.8$ is used in the MCC calculation; the pattern tile size is 8×8 pixel and the maximum axial searching distance is 4 pixel. The constant vector field is obtained with RMS errors less than 0.1 m s^{-1}.

The same MCC calculation is also applied to the sequential images of $L_{wn}(551)$, and the retrieved currents are shown in Fig. 6f. Although the $L_{wn}(\lambda)$ can be used to estimate the Chl (Gordon et al., 1983), it is neither considered as organic matter like Chl nor linearly related to the Chl. Particularly, the Chl derived currents and the $L_{wn}(551)$ derived currents are considered as two independent velocity products because they are separately calculated from their own image sequences without using any relations between the Chl and $L_{wn}(551)$. A quantitative measure of how well these two MCC currents agree with each other can be seen in Fig. 7, where we show the number of vector pairs as a function of the velocity differences $\Delta u = u(\text{Chl}) - u(L_{wn}(551))$ and $\Delta v = v(\text{Chl}) - v(L_{wn}(551))$. The currents in Fig. 6e and f have 84,113 and 190,207 valid vectors respectively retrieved from the satellite images with 1666×1166 pixels. The vector pairs entering the comparison are determined only at a limited part of these pixels. Each compared vector pair includes one valid vector from the Chl currents and the other from the $L_{wn}(551)$ currents at the same time. A total of 4285 vector pairs are identified and most of them are distributed in the narrow range of $(-0.1,+0.1)$ m s^{-1} of Δu and Δv (Fig. 7), which indicates that there are high similarities between the velocity field derived from Chl images and the one from $L_{wn}(551)$ images. The two distribution curves are not completely symmetric because the two derived currents have different domain-wide biases. The variances of the velocity difference between the two MCC products are 0.0132 m^2 s^{-2} in u-component and 0.0074 m^2 s^{-2} in v-component, which reconfirm that these two vector fields are very similar one to the other. Also, because of such a high

Table 3
RMS errors and biases of velocity components in the MCC derived currents.

BioCast test	Currents derived from original imagery				Currents derived from interpolated imagery			
	u_{RMS} (m s^{-1})	v_{RMS} (m s^{-1})	u_{bias} (m s^{-1})	v_{bias} (m s^{-1})	u_{RMS} (m s^{-1})	v_{RMS} (m s^{-1})	u_{bias} (m s^{-1})	v_{bias} (m s^{-1})
1	0.032	0.033	+0.030	+0.029	0.058	0.057	+0.013	+0.009
2	0.031	0.028	−0.030	−0.032	0.057	0.055	−0.012	−0.015
3	0.092	0.045	+0.008	+0.022	0.108	0.086	−0.006	+0.009
4	0.043	0.085	+0.021	+0.003	0.089	0.103	+0.015	−0.007
5	0.018	0.001	−0.009	−0.001	0.055	0.011	−0.007	−0.001

similarity existing between the two independent currents retrieved from different ocean color products, there are plenty of matched features that can be collected over the two currents to characterize the real ocean.

Not only do the inter-product similarities of velocity distribution exist between the MCC products of Chl and $L_{wn}(551)$, but they also exist between many other ocean color derived currents such as those of $B_b(551)$, $C(551)$, Z_{eu}_lee, and $R_{rs}(551)$. Specifically, a hypothesis is that these similarities of velocity distribution across multiple MCC currents resulting from different ocean color products are physically linked with the advective processes and thereby can largely represent the surface flow in the real ocean. The less dependent are the two different ocean colors in relation to each other, the more accurately these inter-product similarities may be expected to represent the surface flow. Because the non-advective biological processes are assumed to be negligible on hourly scales, it is clearly evident that these inter-product similarities are dominated by the physical near-surface advection, especially if a multiple of several independent MCC products are involved.

5. Results in the U.S. East and Gulf coasts (USEGC)

5.1. Evaluation with respect to the HFRadar observation

In the past few decades, scientists have been using the HFRadar as a new tool to map the sea surface currents in coastal waters up to 200 km off the shore (Chapman et al., 1997; Glenn, Dickey, Parker, & Boicourt, 2000; Paduan & Graber, 1997; Parks, Shay, Johns, Martinez-Pedraja, & Gurgel, 2009; Shay, Martinez-Pedraja, Cook, & Haus, 2007). To examine the accuracy of our MCC products with respect to the observation provided by the HFRadar, we focus on several selected sub-regions in the East and Gulf coasts where both the VIIRS overpasses and HFRadar currents are frequently available. Sea surface velocities are measured by the HFRadar through a distributed network, and the synoptic maps of currents are produced in near real-time throughout the coastal waters with the quality control metrics implemented at various stages of data processing. Data in hourly scales are regularly available in several spatial resolutions: 500 m, 1 km, 2 km and 6 km (http://cordc.ucsd.edu/projects/mapping/maps/), while the coverage and availability of the HFRadar currents are not identical over the different resolutions in space. In the present study, we mainly use the 6 km measurements to evaluate the performances of the MCC estimated currents that are possibly subject to various factors and uncertainties such as the intrinsic parameters prearranged in the algorithm, and the type and quality of the source images.

Fig. 8 presents an example of the HFRadar currents versus the currents estimated by the MCC algorithm in the open water outside of the Chesapeake Bay. The dashed line box describes the area shared by both the HFRadar observed currents and the MCC derived currents. The velocity distributions of the two current products are clearly different from each other, but there are still quite a few overlapped grids on which velocity vectors may be compared grid by grid between the two currents. Because the two currents have different coordinate grids, the HFRadar observations are bi-linearly interpolated to the locations of MCC vectors before the comparison is executed.

As mentioned in Section 2, the VIIRS has about 20 different ocean color products as potential candidates for the retrieval of currents. The large family of VIIRS ocean color products provides plenty of information about scattering, absorbance, and resulting optical properties of water, such as color and transparency. Some of these candidate products are heavily influenced by biological processes such as Chl. There are also some in-organic features (e.g., surface salinity) and other properties that are integrated with both organic and in-organic matters, including the B_b, A_t, Z_{eu}, R_{rs} and so on. These products present different features of scattering and particle absorption. Linear dependences are not generally observed between one and the other in any two out of the ~20 ocean color products. Other than the fact that the MCC currents retrieved from different ocean color imagery are independent or weakly dependent of each other, there are also the questions of which color products are best suited to estimate the surface currents and why some are better than the others.

Presented in Fig. 9a and b are the RMS errors in multiple MCC velocity products with respect to the HFRadar currents on several selected days in 2013. The RMS errors in the model currents of the 1/12° operational global Hybrid Coordinate Ocean Model (HYCOM) are also included. The statistics are calculated in the domain approximately ranging from 78.1°W to 71.9°W and 33.6°N to 39.8°N. A total of seven selected ocean color products are compared one to the others, including $A_t(551)$, $B_b(551)$, $C(551)$, Chl, $K_d(490)$, $R_{rs}(551)$, and Z_{eu}_lee. The top three products with the leading performances can be identified as the $R_{rs}(551)$, $B_b(551)$ and $C(551)$. Particularly the currents of the $R_{rs}(551)$ have the smallest RMS errors throughout almost all the days in both the zonal and meridional velocities. Given that the flow speed in the region outside of the Chesapeake Bay can usually go up to ~1.5 m s^{-1} and the average speed can exceed 0.5 m s^{-1}, the overall performances

Table 4
RMS errors and biases of magnitude and direction in the MCC derived currents.

BioCast test	Currents derived from original imagery				Currents derived from interpolated imagery			
	$\|\mathbf{U}\|_{RMS}$ (m s^{-1})	θ_{RMS} (°)	$\|\mathbf{U}\|_{bias}$ (m s^{-1})	θ_{bias} (°)	$\|\mathbf{U}\|_{RMS}$ (m s^{-1})	θ_{RMS} (°)	$\|\mathbf{U}\|_{bias}$ (m s^{-1})	θ_{bias} (°)
1	0.038	5.1	−0.041	+0.1	0.057	11.9	−0.009	+0.8
2	0.034	4.7	−0.042	−0.2	0.055	11.9	−0.014	−0.3
3	0.073	6.1	−0.006	+1.3	0.096	8.5	−0.004	−0.1
4	0.068	5.7	−0.009	−1.1	0.091	8.6	−0.008	−0.3
5	0.018	0.2	−0.009	−0.1	0.055	1.5	−0.007	−0.1

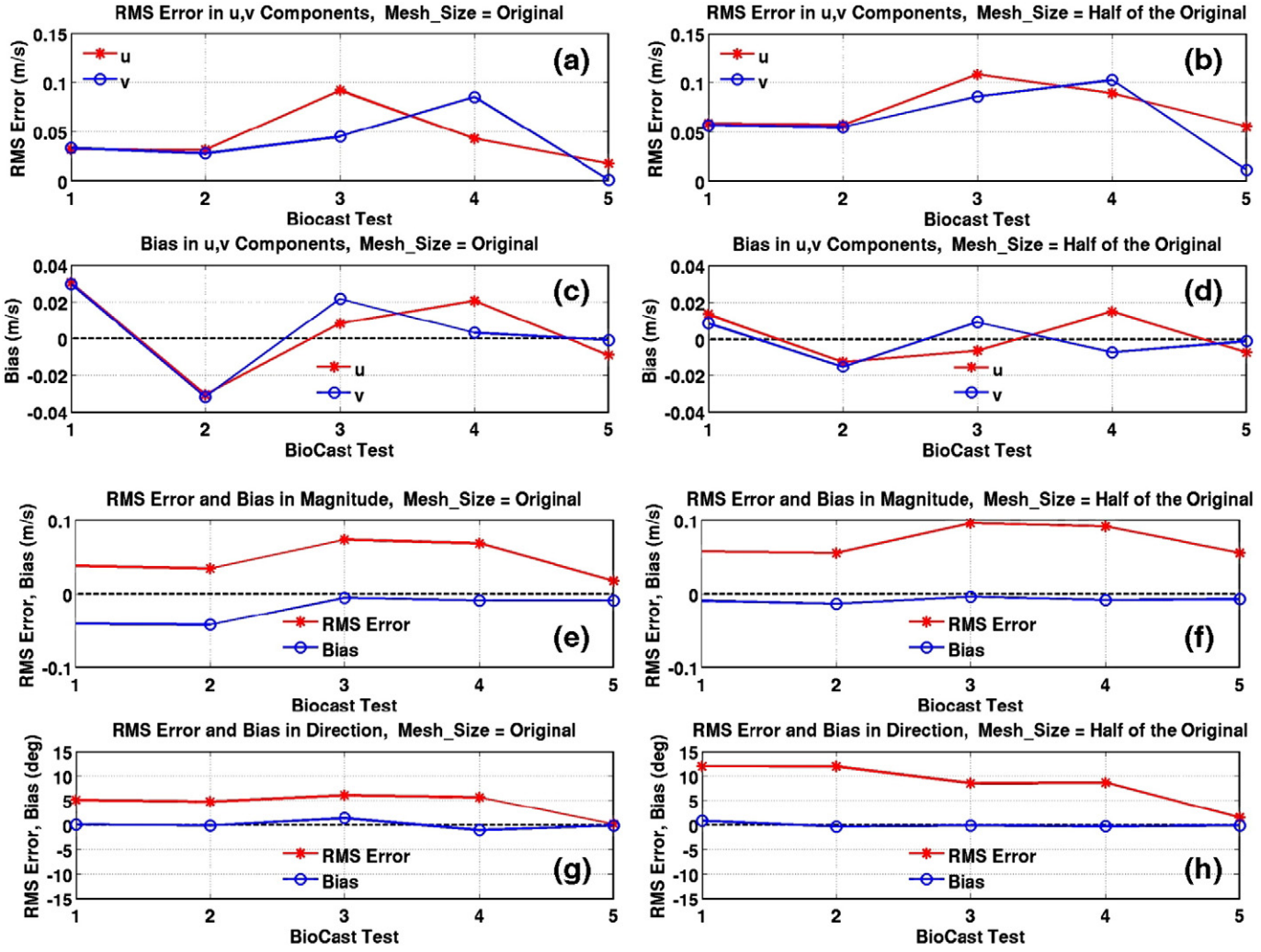

Fig. 5. RMS errors and biases in the MCC currents retrieved from a total of five artificial image sequences loaded with different predetermined velocities (see details in Table 2). The horizontal axes are the test IDs from 1 to 5.

of the seven selected ocean colors are all excellent by yielding the RMS errors smaller than 0.17 m s^{-1}. It is also clearly evident that the performances in our three best products are way better, particularly in the meridional velocities, than the performance of the model surface currents provided by the global HYCOM operational run that has assimilated all the available satellite altimeters, satellite and in-situ surface temperature as well as in-situ vertical temperature and salinity profiles. Comparatively, a color product that focuses more on particle scattering may define the more accurate currents than a biological process dominated ocean color product. This is probably because the particles, particularly the suspended constituents, can physically follow better with the advective water mass transport and thus the migration of particles can be more directly reflected in the associated optical features. As for a biological property like the chlorophyll that actively absorbs energy from lights, the bloom and delay are not only closely related to the bulk flow of surrounding waters but also subject to other independent factors such as the change of temperature profile. In Fig. 9c and d, the RMS errors are compared between two established MCC products (i.e. the derived currents of $B_b(551)$ and $R_{rs}(551)$) and a new joint product loaded with the inter-product similarities that are collected between the currents of $B_b(551)$ and $R_{rs}(551)$. To build this joint product, the velocity vectors from the two MCC currents are compared with each other on every pixel within the domain. The vector pairs with the magnitude difference smaller than 0.3 m s^{-1} and the direction difference smaller than 50° are identified as "matched" features and then assembled into a flow field as a subset currents composed of the inter-product similarities. The error trends of the joint flow field are shown as bold solid lines in red in Fig. 9c and d, indicating that the subset currents integrated with the matchup features have smaller errors than each of the individual products that are being compared. In addition to selecting the individual derived currents with top performances for our needs, it is also evidently possible that the joint product loaded only with inter-product similarities could represent better the observed currents than the best individual products. The constraints of $\Delta|\mathbf{U}| < 0.3$ m s^{-1} and $\Delta\theta < 50°$ are tentatively used here as the criteria to determine whether or not a pair of vectors is in good agreement in the cross-product comparison, and the vector pairs with large inconsistencies are excluded in the merging process. The levels of these constraints may be increased to further reduce the RMS errors. The differences between the joint subset currents and each single deterministic (one member) currents are due to the uncertainty in the MCC retrieved products and the inter-product variabilities can reflect the levels of uncertainty.

Satellite retrieved currents from sequential images of ocean color have a major limitation. Estimating current based on surface fronts does not account for the vertical motion. Subduction and upwelling processes can affect the frontal movement, which will result in uncertainty in the derived surface currents. This limitation represents a non-conservation of mass but is not represented in the surface front location during the estimation of currents. Quantifying the impact on derived current products is difficult and remains problematic in the MCC approach.

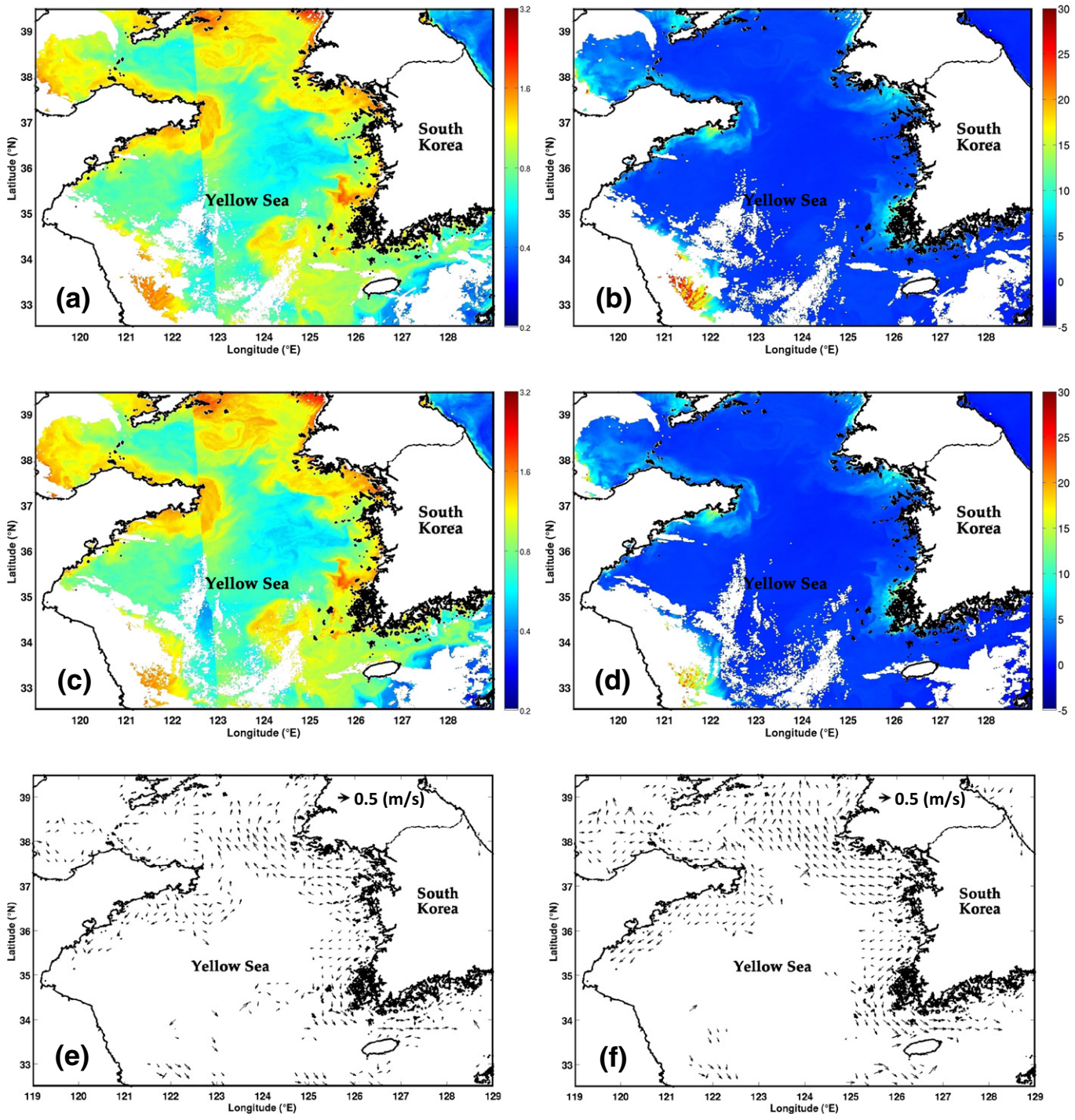

Fig. 6. Sequential GOCI satellite images of (a) Chl at 02:16 UTC, (b) $L_{wn}(551)$ at 02:16 UTC, (c) Chl at 03:16 UTC, (d) $L_{wn}(551)$ at 03:16 UTC on 6 September 2011. The currents in (e) are derived from the Chl images (a) and (c). The currents in (f) are derived from the $L_{wn}(551)$ images (b) and (d). The velocity fields in both (e) and (f) are calculated by MCC algorithm and bin-averaged from a total of 84,113 and 190,207 valid vectors, respectively. The threshold cross-correlation coefficient $k_\sigma = 0.8$ is used in the MCC calculation; the pattern tile is 6×6 pixel and the maximum axial searching distance is 10 pixel. The source images of both the Chl and $L_{wn}(551)$ have 1666×1166 pixels in space with a resolution of approximately 500 m.

Such a limitation is also true in the currents derived from SST fields in the documented studies.

Because the calculation of cross-correlation coefficient is characterized with the pre-established pattern feature and searching criterion (see Eq. 2), the sizes of pattern and search windows may significantly influence on the performance of MCC algorithm during the retrieval of currents. Fig. 10 shows the change of RMS error with the size of search window in the Chesapeake Bay coastal waters for the $B_b(551)$ and Chl. The trends for both the *u*- and *v*-components are presented in the same plot. The search window defines the area where one may expect to find the new location for the original pattern tile after a time delay. It is clearly seen that the currents derived within a larger search window (i.e. the one with an axial searching distance of 18-pixel) almost always achieves a smaller RMS error, but the error reduction is small when the searching distance is increased from 10-pixel to 18-pixel. Such an error reduction is easy to understand, because there might be some cases in which the best cross-correlations are found outside of the 10-pixel searching area but still within the 18-pixel area. However, the computational cost will

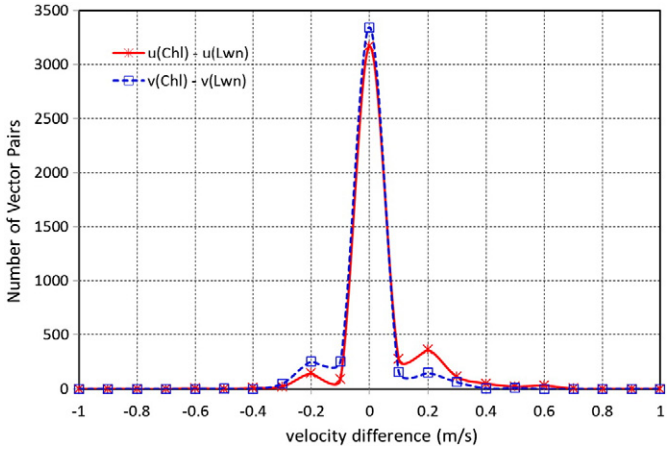

Fig. 7. Comparison between the MCC currents derived from Chl and $L_{wn}(551)$ satellite image sequences. Each of the compared vector pairs has one valid vector from the Chl currents and the other from the $L_{wn}(551)$ currents available on the same pixel. A total of 4285 vector pairs are identified from the two MCC products. The variances of the velocity difference between the two MCC products are 0.0132 $m^2\ s^{-2}$ in zonal velocity u and 0.0074 $m^2\ s^{-2}$ in meridional velocity v. The R-squared value is 0.70 in u and 0.86 in v when $u(\mathrm{Chl}) = u(L_{wn}(551))$ and $v(\mathrm{Chl}) = v(L_{wn}(551))$ are used as the regression lines.

increase exponentially when the searching distance is increased. Therefore, it is necessary to balance carefully the error reduction and the additional computational effort. Across the several tested days, the error trends of Chl are completely different to those of $B_b(551)$. This is because the Chl is a typical biological property, while the $B_b(551)$ is primarily focused on particle scattering. On the other hand, the trends with the larger searching distance follow pretty well those with the smaller searching distance, which implies that these error trends are more likely to be dominated by the type of image instead of the searching criterion in a MCC calculation.

The determination of the optimum template pattern size is related to several important factors. In general, a larger template contains more information for tracking the changes of bio-optical properties and is more statistically significant. However, using the larger template also increases the possibility to include more complicated flow structures such as the rotation and shearing between the fluid layers inside the pattern tile itself. Linear motions of the pattern tile are strongly preferred by the MCC algorithm to obtain a relatively high accuracy in the derived currents. Angular displacement caused by the rotational motions of pattern tile will generally lead to large errors, therefore the strong vorticity effects must be avoided inside the pattern templates as much as possible. We have tested 4 different sizes of the pattern tile in the USEGC studies, and the order of performance with respect to the best accuracy was 4×4 pixel template > 10×10 pixel template > 8×8 pixel template > 6×6 pixel template. Although the 4×4 pixel template has the best performance in both the u- and v-components, the increasing template size does not always lead to the increase of errors. For example, the second best performance corresponds to the 10×10 pixel template instead of the 6×6 or 8×8 one, which has made the impacts of the template size more complicated. As far as the documented studies are reviewed, there is no a unique answer with regard to the optimal selection of the template size, which is more likely to be region-dependent and associated with the quality of source images. Working with *hourly* overlap data is one important reason why these small pattern tiles can work well with the retrieval of currents. In the present study, we use the 4×4 pixel pattern tile in the USEGC tests if not otherwise specified.

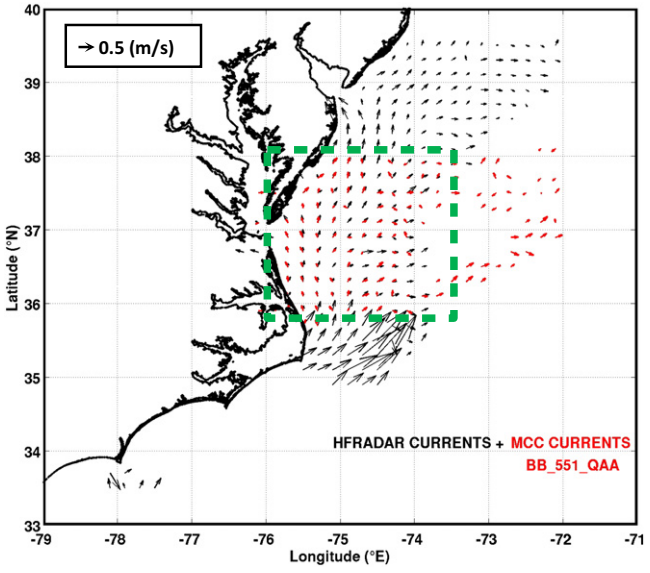

Fig. 8. The comparison of the HFRadar currents and the MCC currents retrieved from the $B_b(551)$ color product in the coastal region outside of the Chesapeake Bay during 17:04–18:44 UTC on June 1st, 2013. The dashed line box describes the area shared by both the HFRadar and the MCC derived currents. The vectors are bin averaged. The bin size is $0.2° \times 0.2°$, which is approximately 18×18 km in this area. In the evaluation of the USEGC velocity products, the RMS errors and biases are calculated over a large data sample before the bin averaging.

5.2. On the production capacity of velocity vectors

In Fig. 11, we compare two groups of ocean color products their vector production capacities by counting the total number of valid velocity vectors resulting from the same sort of MCC implementation. The production capacity quantitatively measures the volume of vectors that can be extracted from the imagery data of a specific ocean color product. Usually the more valid vectors can a color product obtain, the more suited this product is to derive the currents for the estimation of surface advection. This capacity is primarily determined by the volume of useful information and the detailed features of spatial gradients in the imagery of ocean colors. The products in Fig. 11a are mostly the same to those previously mentioned in Fig. 9, including $A_t(551)$, $B_b(551)$, C(551), Chl, $K_d(490)$, Z_{eu}_lee, $R_{rs}(551)$ and salinity. Evidently the ocean color imagery of the $B_b(551)$, C(551) and Z_{eu}_lee is most capable of producing the MCC vectors. Each of the three trends follows fairly closely the other two. The order of performances, however, is subject to the threshold value specified for the minimum requirement of MCC coefficients. For example, if we set a lower expectation of the MCC currents such as $k_\sigma \leq 0.7$, the Z_{eu}_lee provides the best production capacity of valid vectors, while if we increase the cutoff correlation level to k_σ = 0.8–0.9, the leading performance will switch to the $B_b(551)$. Also, the increasing value of k_σ results in the fewer valid vectors in all cases. The two biological ocean color products, namely, the $A_t(551)$ and Chl, present very similar trends of the vector production. The surface salinity product, which represents the dissolved salt contents in the surface water, exhibits a very limited capability of deriving the currents. The velocity field extracted from the surface salinity has more bad vectors than other derived currents especially near the coasts where rivers enter the ocean. Overall, the ocean color products with more influence of scattering and suspended particles are capable of producing more MCC vectors than those heavily influenced by biological processes.

As far as the $R_{rs}(\lambda)$ in multiple bands are concerned, the strongest signals are obtained when the waveband is located near 551 nm and thus $R_{rs}(551)$ has the best vector production capacity among the five ocean color products of $R_{rs}(\lambda)$ (λ = 410, 443, 486, 551, 671 nm, as presented in Fig. 11b). The features of the R_{rs} are determined by the optical properties of the water and its dissolved and particulate constituents. The five products with different wavebands express how the light in each of the several wavebands is reflected from the sea surface depending on

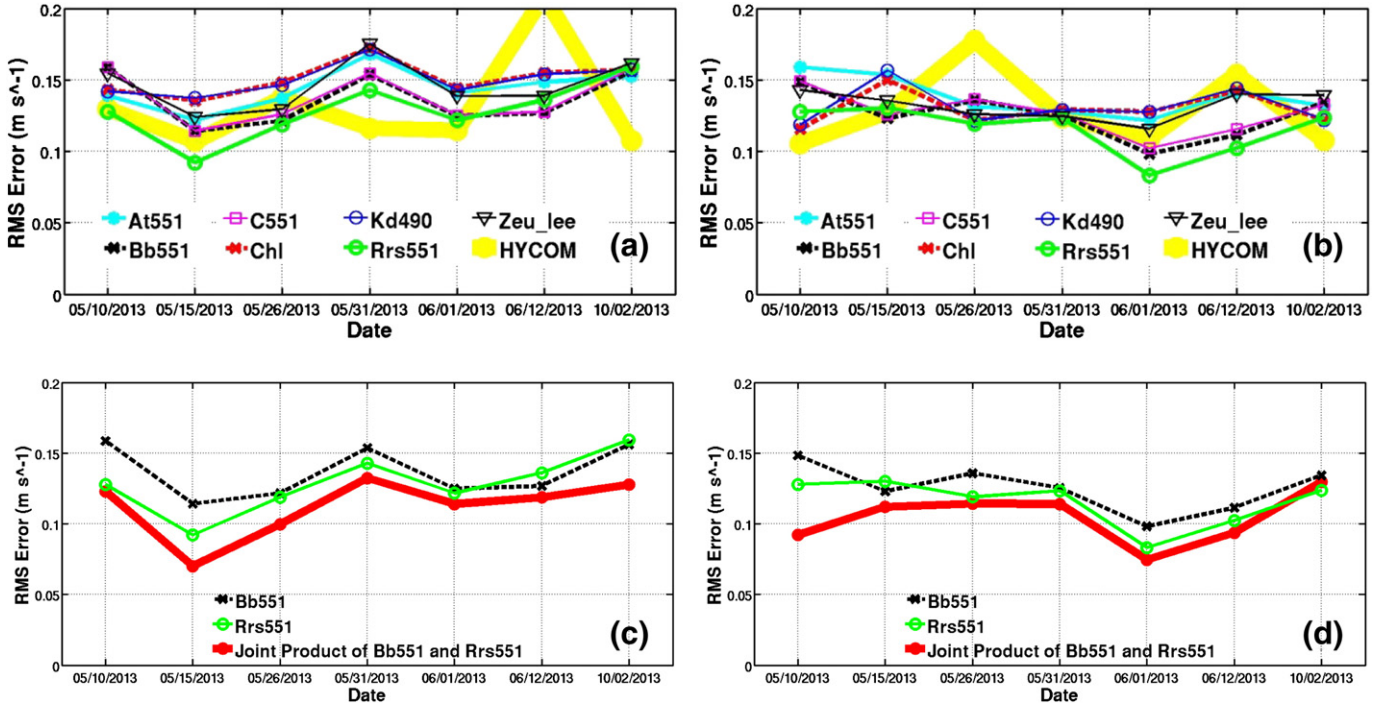

Fig. 9. Top panels show the RMS errors in the (a) *u*-component and (b) *v*-component of multiple MCC velocity products derived from several different color products of the VIIRS satellite as well as the model currents of the 1/12° Navy's operational global Hybrid Coordinate Ocean Model (HYCOM). Bottom panels present the RMS errors in the (c) *u*-component and (d) *v*-component of $B_b(551)$, $R_{rs}(551)$ derived currents and their joint product that is loaded with only the inter-product similarities between the $B_b(551)$ derived currents and the $R_{rs}(551)$ derived currents.

the concentration of sediments in the ocean. Specifically, the reflectance level is associated with a group of optically active components such as phytoplankton pigments (including Chl), organic and mineral suspended particulate matter, and colored dissolved organic matter (CDOM). The increasing Chl usually causes higher reflectance across the visible and near-infrared spectrum, while the impacts of CDOM on the reflectance are case dependent in coastal waters. Fig. 11b is obtained in the area outside of the Chesapeake Bay, where the Chl values are mostly in the level of ~1.0 mg m^{-3} but no larger than 5.0 mg m^{-3} and the R_{rs} spectra have a quite strong peak at 551 nm because of the minimal phytoplankton absorption. The strong signals enabled the $R_{rs}(551)$ color product to yield the largest quantity of velocity vectors. By examining the slopes of curves in Fig. 11b, the vector productivities of $R_{rs}(551)$ and $R_{rs}(671)$ decrease much less with the increase of k_c compared to the other three, indicating that large percentages of the signals of $R_{rs}(551)$ and $R_{rs}(671)$ are closely associated with the movement of water masses and the cross-correlation resulting from these signals are consistently high. By contrast, however, most of the signals in the products of $R_{rs}(410)$, $R_{rs}(443)$ and $R_{rs}(486)$ result in low levels of cross-correlation, showing less capabilities of establishing strong agreement between the advective flow and the pattern shifts of ocean colors.

6. Combination of multiple currents

As mentioned in the previous sections, the MCC current products derived from different ocean color products may carry similarities across the different currents and the inter-product similarities themselves could represent the surface advection more accurately than each single piece out of the multiple derived velocity fields. However, a joint product composed of only the inter-product similarities quantitatively has much less valid vectors than the individual MCC products because most of vectors are denied by the filtering criteria of $\Delta|\mathbf{U}|$ and $\Delta\theta$ as described in Section 5.1. Also, because such a joint product is actually a subset collected from the multiple individual products, it usually has a reduced coverage of the vectors in space and thus has limited practical use. On the other hand, since the gradient distributions have strong impacts on the performance of MCC currents and the different ocean color imagery may have their own large gradients distributed at

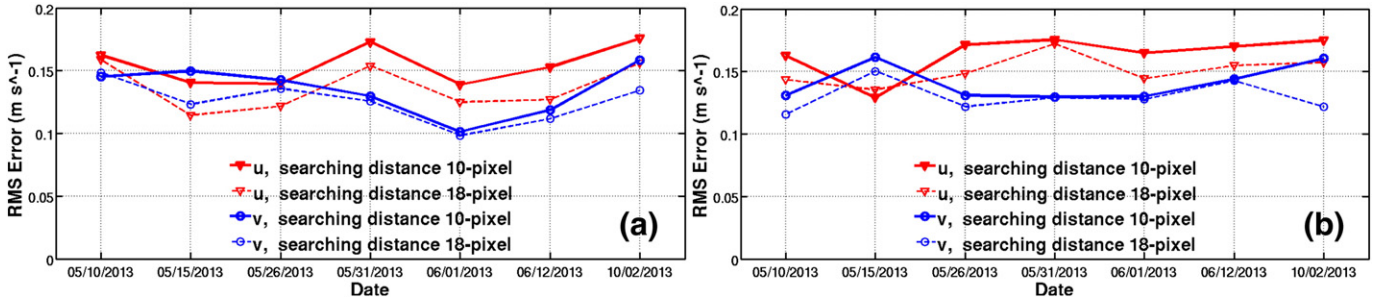

Fig. 10. RMS errors in the MCC currents derived from the imagery of (a) $B_b(551)$ and (b) Chl. The solid line and dashed line trends are corresponding to a maximum axial searching distance of 10-pixel and 18-pixel, respectively.

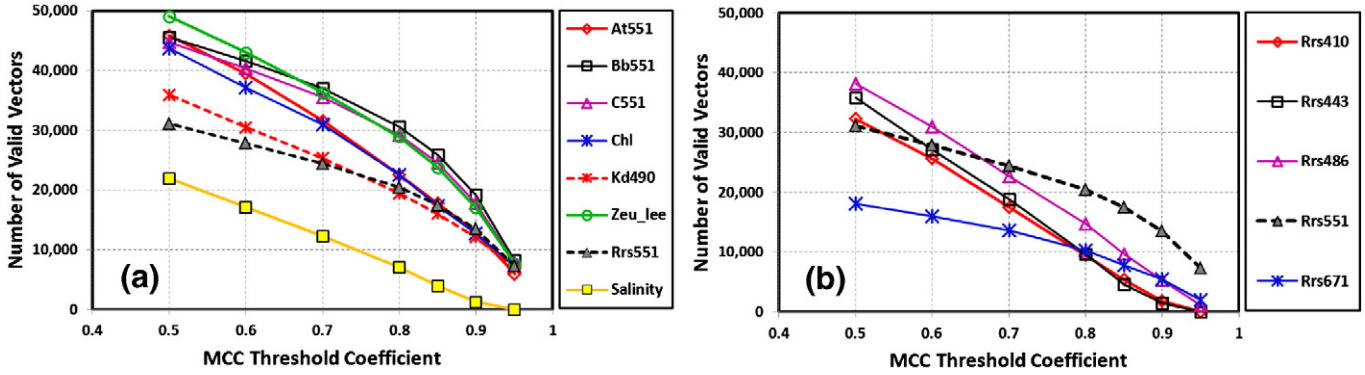

Fig. 11. Comparison of the numbers of valid vectors in the MCC currents resulting from different ocean color products in the group of (a) $A_t(551)$, $B_b(551)$, C(551), Chl, $K_d(490)$, Z_{eu}_lee, $R_{rs}(551)$, salinity, and (b) $R_{rs}(410)$, $R_{rs}(443)$, $R_{rs}(486)$, $R_{rs}(551)$, $R_{rs}(671)$.

different locations in the image space, we can thereby combine the multiple MCC products with similarities without enabling the filters of $\Delta|\mathbf{U}|$ and $\Delta\theta$. That is to say, we may mathematically build one current product from several individually retrieved MCC products by keeping both their inter-product similarities and differences. Below we will discuss the methods for such a combination of multiple MCC products so that an increased total spatial coverage may be obtained for the vector array.

An image derived product by MCC is mathematically a two-dimensional matrix of vectors distributed on the pixels within the entire overlapped area of the sequential images. Vectors are not determined if the pixels are on the lands or the levels of cross-correlation fall below the threshold k_σ. Every retrieved vector has its own cross-correlation coefficient representing a degree of confidence and a quantitative measure of how well the pattern matchup is correlated between two time-lapsed patterns. Based on these correlation coefficients, we propose a weighted simple model to merge multiple image-derived current products. Assume that we have N ($N \geq 2$) products to combine. On a specified pixel (i, j), there are correspondingly N vectors, each of which is from one of the N products and has a cross-correlation coefficient $k_{i,j}^n$ ($i = 1, 2, 3, \ldots$, i-dimension; $j = 1, 2, 3, \ldots$, j-dimension; $n = 1, 2, 3, \ldots, N$). Note that the N vectors on the pixel (i, j) may contain some invalid vectors. To exclude the contribution of those invalid vectors, we introduce the "effective" cross-correlation coefficient $c_{i,j}^n$, which is defined as,

$$c_{i,j}^n = \begin{cases} k_{i,j}^n, & \left(k_{i,j}^n \geq k_\sigma\right) \\ 0, & \left(k_{i,j}^n < k_\sigma\right) \end{cases}. \tag{3}$$

Based on $c_{i,j}^n$, the combined velocity on the pixel (i, j) is then calculated by,

$$\mathbf{U} = \sum_{n=1}^{N}\left(c_{i,j}^n \cdot \mathbf{U}_{i,j}^n\right) \Big/ \sum_{n=1}^{N}\left(c_{i,j}^n\right), \tag{4}$$

where $\mathbf{U}_{i,j}^n$ is the vector provided by the nth velocity product for the pixel (i, j). An example for merging multiple MCC currents with the above method is given in Fig. 12. The MCC currents derived from the Chl and

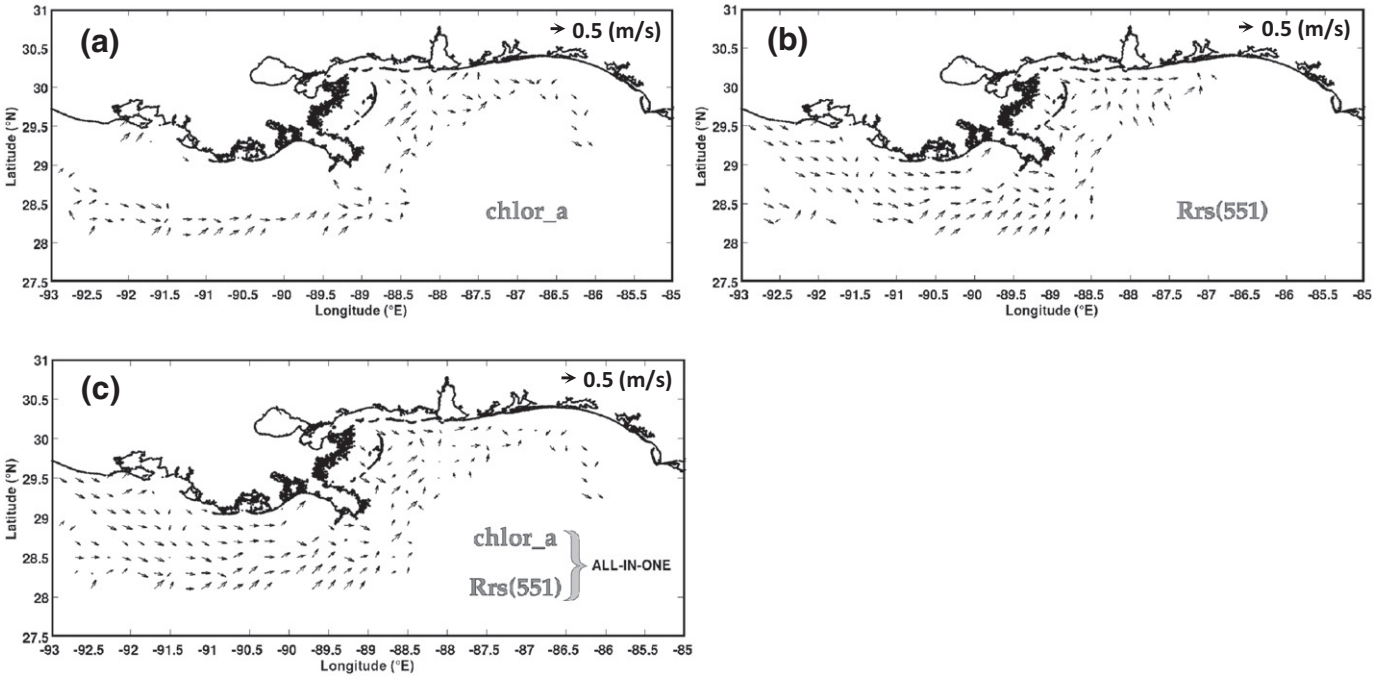

Fig. 12. Individual looks of multiple MCC currents retrieved from the VIIRS satellite images of (a) Chl and (b) $R_{rs}(551)$ during 18:09–19:51 UTC on May 7th, 2013. The two derived MCC products are merged by Eq. (4) to obtain the currents as shown in panel (c), which has an increased total spatial coverage of vectors compared to each of the individual vector arrays in panel (a) or (b).

$R_{rs}(551)$ imagery are shown in Fig. 12a and b, respectively. Both the Chl and $R_{rs}(551)$ products are provided by the VIIRS orbital overlaps in the Northern Gulf of Mexico. The vector coverages of their derived currents are clearly different from each other. The $R_{rs}(551)$ has strong signals near the shore of the Louisiana–Mississippi shelf and therefore has plenty of vectors retrieved in this area. The Chl has its strongest signals further off the shore and extended approximately to 86°W. The combining procedure collects the contributions of both participants and ensembles them into a single flow field as shown in Fig. 12c. The joint product constructed from the MCC currents of $B_b(551)$ and $R_{rs}(551)$, which corresponds to the bold solid lines in Fig. 9c and d, is also resulting from this method but additionally filtered by the constraints of $\Delta|\mathbf{U}| < 0.3$ m s^{-1} and $\Delta\theta < 50°$ between the two vector arrays.

Other than the simple model described above, efforts are also underway to blend together the multiple flow fields by using the flow decomposition and reconstruction procedure proposed by Chu, Ivanov, Margolina, Korzhova, and Melnichenko (2003a,b). Based on two scalar potentials identified as toroidal and poloidal, it decomposes the scatteredly distributed velocities into a spectral representation integrated with a group of velocity basis functions, some constant coefficients, and a spectrally varying parameter κ associated with the homogeneous open boundary conditions. In our on-going studies, one choice of estimating the open boundary condition is to use the boundary velocity values from the Navy's HYCOM operational model. In contrast to the one described in Eqs. (3) and (4), this procedure is a more general one that may further be extended to combine the image-derived currents with any other independently available currents such as the HFRadar velocity observations or the ocean model generated velocity products within the shared domain. The combination of the image-derived currents and the HFRadar currents would greatly extend the coverage of the coastal observation system without additionally deploying expensive instruments. In general, the procedure for merging multiple currents provides a vigorous platform to collect credits from different ocean colors or different algorithms, and the idea is somewhat similar to the conventional ensemble method in statistics. The merging of multiple current products can improve the results by allowing diversity and more flexibility in their representation of the near-surface advection.

7. Concluding remarks

Sequential satellite ocean color images on hourly scales are used to extract the near-surface currents by the MCC algorithm. We not only demonstrate the retrieval of currents from the geostationary satellite ocean color products but also present for the first time that the overlap of sensor swath between the VIIRS sequential orbits can be used to estimate the near-surface advection. The retrieval calculations are validated in several test cases of the BioCast experiment and the image-derived products are evaluated with respect to the HFRadar measurements in the USEGC. The RMS errors in our best derived currents from the VIIRS ocean color overlaps are less than 0.17 m s^{-1} in the evaluation area outside of the Chesapeake Bay. The most accurately derived currents are from the imagery of $R_{rs}(551)$, $B_b(551)$ and C(551). The image sequences of $B_b(551)$ and Z_{eu}_lee are capable of yielding the largest quantities of velocity vectors. It is clearly evident that the errors in our top-performing MCC currents from ocean color products are way smaller than those in the model generated currents provided by the 1/12° global HYCOM data assimilative experiment. Multiple derived currents from different ocean colors are cross compared to learn the differences dominated by individual bio-optical properties and the similarities that are more likely to be linked with the near-surface advection. The subset currents that are assembled with only the inter-product similarities collected between different MCC derived currents may present reduced errors compared to each of the individual products. Errors and bad vectors may be reduced by smoothing the source images and applying several types of filters during the post-processing. Attempts are also made to combine multiple image-derived products to increase the spatial coverage of velocity vectors. In some coastal waters where the velocity observations are limited, the image-derived currents can significantly increase our knowledge of the near-surface circulation and support various operational activities. Similar to the HFRadar products, the currents derived from ocean colors may also contribute to the data assimilation in ocean circulation models, the studies of coastal ecosystems, the near real-time ship navigation and adaptive sampling, as well as the search-and-rescue operations. Given that the satellite-based remote-sensing is being used increasingly for regional-scale assessments of optically related characteristics in coastal waters, it may be expected that the ocean color imagery derived surface currents would play a more significant role in many of the coastal activities in the future.

Acknowledgments

Financial support was provided by the Naval Research Laboratory, BAA Award Number N00173-09-2-C903 to the University of Southern Mississippi. Appreciation is extended to Ryan Vandermeulen for VIIRS data. We are grateful to the anonymous reviewers for their helpful comments and suggestions.

References

Arnone, R., Ladner, S., Fargion, G., Martinolich, P., Vandermeulen, R., Bowers, J., et al. (2013). Monitoring bio-optical processes using NPP-VIIRS and MODIS-Aqua ocean color products. *Proc. SPIE 8724, Ocean Sensing and Monitoring V* (pp. 87240Q). http://dx.doi.org/10.1117/12.2018180.

Baker, N. (2011). Joint Polar Satellite System (JPPS) VIIRS Geolocation Algorithm Theoretical Basis Document (ATBD). http://npp.gsfc.nasa.gov/science/sciencedocuments/ATBD_122011/474-00053_Geolocation_ATBD_Rev-_20110422.pdf

Bannehr, L., Rohn, M., & Warnecke, G. (1996). A functional analytic method to derive displacement vector fields from satellite image sequences. *International Journal of Remote Sensing, 17*(2), 383–392.

Chapman, R.D., Shay, L.K., Graber, H.C., Edson, J.B., Karachintsev, A., Trump, C.L., et al. (1997). On the accuracy of HF radar surface current measurements: intercomparisons with ship-based sensors. *Journal of Geophysical Research, 102*, 18737–18748.

Chen, W., Mied, R.P., & Shen, C.Y. (2008). Near-surface ocean velocity from infrared images: Global Optimal Solution to an inverse model. *Journal of Geophysical Research, 113*(C10). http://dx.doi.org/10.1029/2008JC004747.

Chu, P.C., Ivanov, L.M., Margolina, T.M., Korzhova, T.P., & Melnichenko, O.V. (2003a). Analysis of sparse and noisy ocean current data using flow decomposition, part 1, theory. *Journal of Atmospheric and Oceanic Technology, 20*, 478–491.

Chu, P.C., Ivanov, L.M., Margolina, T.M., Korzhova, T.P., & Melnichenko, O.V. (2003b). Analysis of sparse and noisy ocean current data using flow decomposition, part 2, applications to Eulerian and Lagrangian data. *Journal of Atmospheric and Oceanic Technology, 20*, 492–512.

Cote, S., & Tatnall, A.R.L. (1994). Estimation of sea surface velocities from space using neural networks. *Proc. SPIE 2315. Image and Signal Processing for Remote Sensing, 444*, . http://dx.doi.org/10.1117/12.196744.

Crocker, R.I., Matthews, D.K., Emery, W.J., & Baldwin, D.G. (2007). Computing coastal ocean surface currents from infrared and ocean color satellite imagery. *IEEE Transactions on Geoscience and Remote Sensing, 45*(2), 435–447.

Dickey, T., Marra, J., Granata, T., Langdon, C., Hamilton, M., Wiggert, J., et al. (1991). Concurrent high resolution bio-optical and physical time series observations in the Sargasso Sea during the spring of 1987. *Journal of Geophysical Research, 96*(C5), 8643–8663.

Emery, W.J., Fowler, C., & Clayson, C.A. (1992). Satellite-image-derived Gulf Stream currents compared with numerical model results. *Journal of Atmospheric and Oceanic Technology, 9*, 286–304.

Emery, W.J., Thomas, A.C., Collins, M.J., Crawford, W.R., & Mackas, D.L. (1986). An objective method for computing advective surface velocities from sequential infrared satellite images. *Journal of Geophysical Research, 91*(C11), 12865–12878.

Garcia, C.A.E., & Robinson, I.S. (1989). Sea surface velocities in shallow seas extracted from sequential coastal zone color scanner satellite data. *Journal of Geophysical Research, 94*(C9), 12681–12691.

Glenn, S.M., Dickey, T.D., Parker, B., & Boicourt, W. (2000). Long-term real-time coastal ocean observation networks. *Oceanography, 13*, 24–34.

Gordon, H. R., Clark, D. K., Brown, J. W., Brown, O. B., Evans, R. H., & Broenkow, W. W. (1983). Phytoplankton pigment concentrations in the Middle Atlantic Bight: Comparison of ship determinations and CZCS estimates. *Applied Optics, 22*, 20–36.

Gordon, H.R., & Wang, M. (1994). Retrieval of water-leaving radiance and aerosol optical thickness over the oceans with SeaWiFS: A preliminary algorithm. *Applied Optics, 33*, 443–452.

Horn, B.K.P., & Schunck, B.G. (1981). Determining optical flow. *Artificial Intelligence, 17*, 185–203. http://dx.doi.org/10.1016/0004-3702(93)90173-9.

Jolliff, J.K., Ladner, S., Crout, R., Lyon, P., Matulewski, K., Arnone, R.A., et al. (2014). Forecasting the ocean's optical environment using the BioCast system. *Oceanography, 27*, 46–57.

Jolliff, J.K., Smith, T.A., Ladner, S., & Arnone, R.A. (2014). Simulating surface oil transport during the Deepwater Horizon oil spill: Experiments with the BioCast system. *Ocean Modelling*, *75*, 84–99.

Kamachi, M. (1989). Advective surface velocities derived from sequential images for rotational flow field: Limitations and applications of maximum-cross-correlation method with rotational registration. *Journal of Geophysical Research*, *94*(C12), 18227–18233.

Lee, Z.P., Carder, K.L., & Arnone, R. (2002). Deriving inherent optical properties from water color: A multi-band quasi-analytical algorithm for optically deep waters. *Applied Optics*, *41*, 5755–5772.

Lee, Z.P., Weidemann, A., Kindle, J., Arnone, R., Carder, K.L., & Davis, C. (2007). Euphotic zone depth: Its derivation and implication to ocean-color remote sensing. *Journal of Geophysical Research*, *112*, C03009. http://dx.doi.org/10.1029/2006JC003802.

Matthews, D.K., & Emery, W.J. (2009). Velocity observations of the California Current derived from satellite imagery. *Journal of Geophysical Research*, *114*(C8). http://dx.doi.org/10.1029/2008JC005029.

Paduan, J.D., & Graber, H.C. (1997). Introduction to high-frequency radar: Reality and myth. *Oceanography*, *10*, 36–39.

Parks, A.B., Shay, L.K., Johns, W.E., Martinez-Pedraja, J., & Gurgel, K.W. (2009). HF radar observations of small-scale surface current variability in the Straits of Florida. *Journal of Geophysical Research*, *114*, C08002. http://dx.doi.org/10.1029/2008JC005025.

Shay, L.K., Martinez-Pedraja, J., Cook, T.M., & Haus, B.K. (2007). High-frequency radar mapping of surface currents using WERA. *Journal of Atmospheric and Oceanic Technology*, *24*, 484–503. http://dx.doi.org/10.1175/JTECH1985.1.

Svejkovsky, J. (1988). Sea surface flow estimation from advanced very high resolution radiometer and coastal zone color scanner satellite imagery: A verification study. *Journal of Geophysical Research*, *93*(C6), 6735–6743. http://dx.doi.org/10.1029/JC093iC06p06735.

Vigan, X., Provost, C., Bleck, R., & Courtier, P. (2000a). Sea surface velocities from sea surface temperature image sequences: 1. Method and validation using primitive equation model output. *Journal of Geophysical Research*, *105*(C8), 19499–19514.

Vigan, X., Provost, C., Bleck, R., & Courtier, P. (2000b). Sea surface velocities from sea surface temperature image sequences: 2. Application to the Brazil–Malvinas confluence area. *Journal of Geophysical Research*, *105*(C8), 19515–19534.

Wahl, D.D., & Simpson, J.J. (1989). Velocity estimates from space sensitivity to computational methods and near-surface physical processes. *Oceans '89. Proceedings*, *3*. (pp. 965–970). http://dx.doi.org/10.1109/OCEANS.1989.586715.

Wahl, D.D., & Simpson, J.J. (1990). Physical processes affecting the objective determination of near-surface velocity from satellite data. *Journal of Geophysical Research*, *95*(C8), 13511–13528. http://dx.doi.org/10.1029/JC095iC08p13511.

Wahl, D.D., & Simpson, J.J. (1991). Satellite derived estimates of the normal and tangential components of near-surface flow. *International Journal of Remote Sensing*, *12*, 2529–2571. http://dx.doi.org/10.1080/01431169108955285.

Werdell, P.J., Franz, B.A., Bailey, S.W., Feldman, G.C., Boss, E., Brando, V.E., et al. (2013). Generalized ocean color inversion model for retrieving marine inherent optical properties. *Applied Optics*, *52*(10), 2019–2037.

Wu, Q.X., Pairman, D., McNeill, S.J., & Barnes, E.J. (1992). Computing advective velocities from satellite images of sea surface temperature. *IEEE Transactions on Geoscience and Remote Sensing*, *30*(1), 166–176.

Zavialov, P.O., Grigorieva, J.V., MoLler, Osmar O., Kostianoy, A.G., & Gregoire, M. (2002). Continuity preserving modified maximum cross-correlation technique. *Journal of Geophysical Research*, *107*(C10). http://dx.doi.org/10.1029/2001JC001116 (24-1–24-10).